**Journal of the European Optical
Society-Rapid Publications**

RESEARCH ARTICLE

OPEN ACCESS

Interplay of $\chi^{(2)}$ and $\chi^{(3)}$ effects for microcomb generation

Francesco Rinaldo Talenti[1,2,*], Luca Lovisolo[1,2], Andrea Gerini[2], Huanfa Peng[3], Pedro Parra-Rivas[4],
Tobias Hansson[5], Yifan Sun[6], Carlos Alonso-Ramos[1], Martina Morassi[1], Aristide Lemaître[1],
Abdelmounaim Harouri[1], Christian Koos[3], Stefan Wabnitz[7,8], Laurent Vivien[1], and Giuseppe Leo[2]

[1] Université Paris-Saclay, CNRS, Centre de Nanosciences et de Nanotechnologies, 91120 Palaiseau, France
[2] Laboratoire Matériaux et Phénomènes Quantiques, Université Paris Cité, 75013 Paris, France
[3] Institute of Photonics and Quantum Electronics, Karlsruhe Institute of Technology, 76131 Karlsruhe, Germany
[4] Department of Chemistry and Physics, University of Almeria, 04120 Almeria, Spain
[5] Department of Physics, Chemistry and Biology, Linköping University, Linköping, SE-581 83, Sweden
[6] Service OPERA-Photonique, Université libre de Bruxelles, B-1050 Brussels, Belgium
[7] Dipartimento di ingegneria elettronica e telecomunicazioni, Sapienza University of Rome, 00184 Roma, Italy
[8] CNR-INO, Istituto Nazionale di Ottica, 80078 Pozzuoli, Italy

Abstract. While frequency comb generation in passive nonlinear optical cavities has been demonstrated in purely quadratic and Kerr platforms, the interplay between $\chi^{(2)}$ and $\chi^{(3)}$ effects is yet to be fully understood. In this work, we propose a doubly resonant AlGaAs microring design for second-harmonic Kerr-comb generation. We compute the full dispersion profile of the guided modes to describe the resulting dynamics. The doubly resonant condition implies the use of a double envelope mean-field model, and the confined field owns spectral components around both the pump and second harmonic wavelengths. The fabrication of such devices is discussed, and preliminary experimental results are presented. Due to its record nonlinear performance, we address AlGaAs as a promising platform for the generation of such novel microcomb sources.

Keywords: Optical frequency combs, Second harmonic generation, Nonlinear optics, AlGaAs.

1 Introduction

Optical frequency comb (OFC) generation based on second-harmonic (SH) nonlinear frequency conversion was first demonstrated in a bow-tie optical cavity [1, 2], and a cascade of $\chi^{(2)}$ processes was found to mimic a Kerr effect resulting in a modulation-instability (MI) OFC regime [3]. Besides, Kerr whispering-gallery-mode resonators with a toroidal shape have been used to generate octave-spanning microcombs [4] and temporal cavity solitons (CSs) [5], as predicted a couple of decades earlier [6].

Today, novel architectures have been demonstrated to excite robust CSs dynamical attractors [7], while innovative pumping schemes, such as chirped-pulse pumping, have been proposed to achieve complete control on the CS dynamics [8]. In the same context, on-chip integration of quadratic platforms at the µm-size scale is receiving increasing attention with a view to possibly achieving lower-power pump thresholds [9]. This is witnessed by the recent records of $\chi^{(2)}$ microring optical parametric oscillator (OPO) [10], Pockels micro-comb [11], and bicolor CSs [12].

At the same time, III-V semiconductors have proven interesting for nonlinear optical applications due to their energy bandgap tunability, which provides direct solutions for waveguide-dispersion engineering, and their typically high second- and third-order nonlinear response. As such, they led to paradigmatic demonstrations: SH vortex generation [13] and spin-orbit coupling [14] using nonlinear metasurfaces, entangled-photon sources [15, 16], ultralow-power Kerr OFC [17, 18], and photonic crystal cavity (PhC) OPO [19, 20]. Moreover, second harmonic generation (SHG) has been reported for (Al)GaAs [21–23] and (In)GaP alloys in both type I [24, 25] and type II [16, 26, 27] phase-matching (PM) schemes. Further perspective examples are broadband SHG [28] and electrically injected OPO [29].

Here, to model the OFC generation in a SHG-Kerr cavity [30, 31], we consider a double-envelope mean-field model, as was previously done to describe e.g. the field evolution of SHG [32, 33] and third-harmonic generation (THG) [34] in doubly resonant cavities. With this approach, one can predict Kerr-induced MI [35] and bistable soliton solutions [36] in a waveguide configuration. The case of an

---

OPO resonator was presented in reference [37], and a two-wave model was used to describe the interplay between $\chi^{(3)}$ and $\chi^{(2)}$ surface effects in a silicon-nitride resonator [38]. As a general rule, whenever a non-negligible frequency conversion occurs into far different spectral domains, multi-envelope mean-field models are more convenient [39].

The scheme of our OFC generation setup is shown in Figure 1a. A monochromatic continuous-wave (CW) driving field S, around a resonance frequency $\nu_0 = \omega_0/2\pi$, is coupled evanescently in a SHG-Kerr ring resonator from a bus waveguide. Thanks to quadratic nonlinear effects, an important fraction of power is converted to the SH at $2\omega_0$. The intracavity field consists of two nonlinearly coupled waves (A, B), whose spectral broadening is due to the $\chi^{(2)} + \chi^{(3)}$ interactions. The resulting output OFC owns spectral components around both the carriers ω_0 and $2\omega_0$. Figure 1b provides our technological choice for the waveguide cross-section: an AlGaAs core on top of a SiO_2 cladding and a Si wafer.

In the following, we present the two-wave nonlinear dynamics resulting from the $\chi^{(2)} + \chi^{(3)}$ interplay in AlGaAs waveguides. Since we focus on the relevant case of a pump wavelength in the telecom range, we discuss the crucial problem of the strong normal dispersion in the spectral domain around the SH $\lambda_{SH} \sim 0.775$ µm. A valid solution is represented by a systematic dispersion engineering approach, which exploits local Bragg mirroring effects [40] and resonance frequency splittings [41] in a hybrid PhC-microring system [42]. Novel inverse design techniques of waveguides [43] or microcombs [44] address this specific topic.

The manuscript is organized as follows: in Section 2 we present the design of a doubly resonant AlGaAs microring; in Section 3 we model the resulting SHG-Kerr comb generation dynamics; in Section 4 we propose a purely $\chi^{(2)}$ optical feedback and we model the SHG; in Section 5 we discuss fabrication and present preliminary linear measurements; finally, in Section 6 we draw our conclusions and give some perspectives.

2 AlGaAs ring design

The alloy $Al_{0.18}Ga_{0.82}As$ was chosen to both guarantee a high $\chi^{(2)}$ ($\chi^{(2)}_{xyz} \sim 238$ pm/V at $\lambda \sim 1.55$ µm [45]) and avoid two-photon absorption (TPA) at $\lambda_0 = 1.55$ µm.

The AlGaAs crystal allows to achieve directional quasi phase matching ($\bar{4}$-QPM) between guided modes at ω_0 and $2\omega_0$ [46, 47], and the main design parameters are the waveguide width w, height h and bending radius R. Since optimal dispersion for Kerr-comb excitation around ω_0 occurs for waveguide cross sections with $(h, w) \sim (400, 600)$ nm [17, 18], we investigate geometries with $h = 400$ nm and we let w free to vary around its optimum.

2.1 Phase matching and frequency doubling efficiency

We make use of a commercial software (Lumerical, package FDE [48]) to compute the waveguide eigenmodes and their effective index (n_{eff}). A modal PM condition between fundamental transverse modes (either TE_{00} or TM_{00}) at
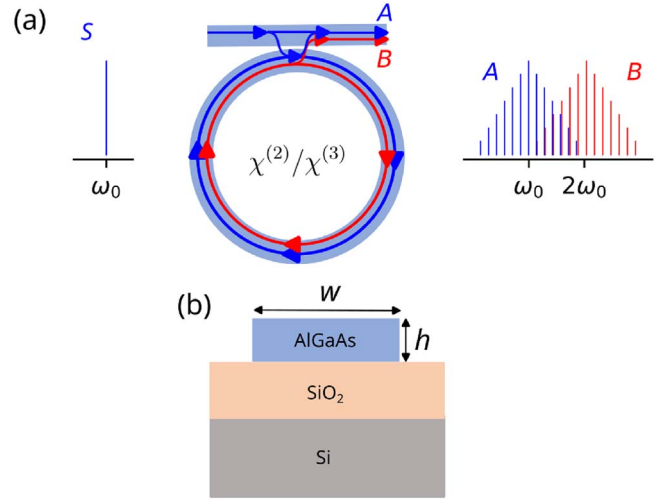

Figure 1. (a) Scheme of a passively driven doubly resonant SHG-Kerr ring resonator. (b) Transverse cross-section with height h and width w.

the driving wavelength and a higher-order transverse mode (TE_{02}) at SH is found. The energy density of the phase-matched eigenmodes is reported in Figure 2a, while Figure 2b reports the PM diagram of n_{eff} as a function of the waveguide width. The blue marker corresponds to a type-II PM point, found for $w \sim 470$ nm. This occurs as the average of the n_{eff} of two pump modes (black dashed line) equals the n_{eff} of the SH mode. The red marker indicates a type-I PM point (found for $w \sim 610$ nm), which occurs whenever the effective index of the pump mode is equal to that of the SH.

We next compute the SHG efficiency [25, 26]:

$$\kappa = \frac{\omega_0 \epsilon_0}{4} \int_\Omega \chi^{(2)}_{xyz} \mathbf{e}^{x,*}_{2\omega_0} \left(\mathbf{e}^y_{\omega_0,1} \mathbf{e}^z_{\omega_0,2} + \mathbf{e}^y_{\omega_0,2} \mathbf{e}^z_{\omega_0,1} \right) d\Omega, \qquad (1)$$

where $\mathbf{e}_{\omega_0,1}$, $\mathbf{e}_{\omega_0,2}$ and $\mathbf{e}_{2\omega_0}$ are the electric fields at ω_0 and $2\omega_0$, respectively, $\mathbf{\Omega}$ is the waveguide cross-section, $\chi^{(2)}$ is the second order susceptibility tensor, ϵ_0 is the electric permittivity, and x, y and z are the spatial coordinates. The symbol * indicates the complex conjugate, and tensor index contraction follows the Einstein summation convention. In equation (1) we use the standard normalization $\mathbf{e}_{norm} = \mathbf{e}/\sqrt{N}$ [25], with $N = (1/2) \int (\mathbf{e} \times \mathbf{h}^*) \cdot \hat{\mathbf{x}} \, d\Omega$, $\mathbf{h}$ the magnetic field, x the propagation direction and $\times$ the vector product. Since $\chi^{(2)}_{xyz}$ is a tensor, κ is strongly influenced by the orientation of the propagation direction with respect to the crystalline axes. For this reason we define θ as the angle, in the (001) plane, between the propagation direction and the [100] axis. The SHG generation efficiency $|\kappa|^2$ is reported in Figure 2c for both type-I and type-II PM conditions. We note that the κ assumes comparable values in these two cases. In what follows we will consider the type-I PM case for two main reasons: 1) it results in a better dispersion profile; 2) for the type-II modal PM we are close to a degeneracy point $w = h$, which is detrimental for broadband applications. Finally, as introduced above, in a ring configuration the condition $\bar{4}$-QPM implies slightly different optimal w. The corresponding waveguide cross-section is thus set as $(w, h) = (630, 400)$ nm.
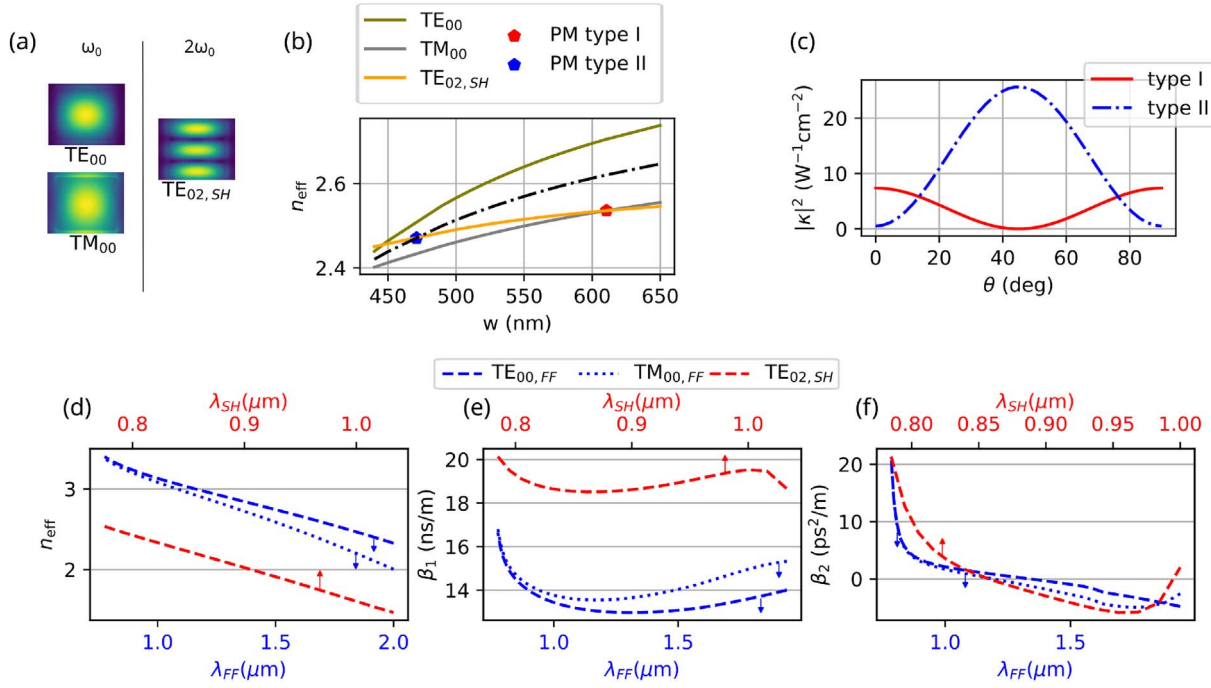
Figure 2. (a) Energy density of the phase-matched guided modes at ω_0 (TE$_{00}$ and TM$_{00}$) and $2\omega_0$ (TE$_{02,SH}$). (b) n_{eff} vs. w diagram of type-I (red marker) and type-II (blue marker) modal PM. (c) SHG efficiency as a function of the angle θ between the propagation direction and the [100] axis. (d) Effective index n_{eff}, (e) group velocity β_1, and (f) GVD β_2 for the TE$_{00,FF}$ (blue dashed line), TM$_{00,FF}$ (blue pointed line) and TE$_{02,SH}$ modes (red dashed line). In (d, e, f) the colored arrows indicate the corresponding x-axis.

2.2 Chromatic dispersion

Chromatic dispersion plays a pivotal role for broadband frequency generation, as the propagation constant has a different spectral dependence for each mode. It is convenient to expand it in Taylor series around a carrier frequency ω_0 [49]:

$$\beta(\omega) = n_{\text{eff}}(\omega)\frac{\omega}{c} = \sum_k \beta_k \frac{[\omega - \omega_0]^k}{k!}, \qquad (2)$$

where $\beta_k = \left[\mathrm{d}^k\beta/\mathrm{d}\omega^k\right]_{\omega=\omega_0}$; β_1^{-1} is the group velocity and β_2 the group velocity dispersion (GVD). In a mean-field approximation, which has been largely proven to accurately describe the physics of OFC generation [50], the crucial quest for spectral broadening is that of anomalous dispersion, i.e. $\beta_2 < 0$. This is meant to compensate and balance nonlinear effects, directly responsible for the formation of novel spectral components. Moreover, a small $|\beta_2|$ is typically preferable to minimize the OPO power threshold. In the ideal case, the target is $\beta_2 < 0$ and $|\beta_2| \sim 0$ in a large spectral domain.

When SHG effects are non negligible, a substantial part of the driving field might be converted into the SH spectral domain. Under the doubly resonant condition, the energy carried by the SH wave remains confined in the optical cavity. In such situations, a double-envelope model provides accurate and physically consistent descriptions [39]. This considers two mean-field equations coupled by Kerr and SHG terms, describing the field evolution around the fundamental frequency (FF) and the SH components,

respectively, with different propagation constants β_{FF} and β_{SH}. In a doubly resonant SHG-Kerr cavity, besides the usual requirement of anomalous GVD for both $\beta_{2,\text{FF}}$ and $\beta_{2,\text{SH}}$ around FF and SH, also the corresponding group velocities $\beta_{1,\text{FF}}$ and $\beta_{1,\text{SH}}$ must take on prescribed values. In particular, the group velocity mismatch $\Delta\beta_1 = \beta_{1,\text{SH}} - \beta_{1,\text{FF}}$ must be moderately small, or ideally zero [32]. To model realistic situations, it is crucial to incorporate a detailed representation of dispersive effects into the dynamics. For this reason, we compute the full dispersion profiles for the phase-matched modes, and Figures 2d–2f reports n_{eff}, β_1 and β_2 around ω_0 and $2\omega_0$. It is apparent that we have anomalous dispersion at ω_0 but not at $2\omega_0$. In the next section, we will see how this is detrimental for CS generation.

It is worth to mention that, beyond the propagation constant, other parameters exhibit a non-zero chromatic dispersion. For instance, variations in the waveguide mode profiles over a broad spectral domain could slightly affect the resulting dynamics [51]. In this work, we neglect these effects for simplicity, and we ascribe all the dispersive effects of the underlying dynamics solely to $\beta(\omega)$.

3 OFC dynamics

3.1 The model

Let us consider the system of two mean-field equations passively driven and damped, coupled by means of nonlinear Kerr and SHG terms [32, 33, 38, 52]:

$$\frac{t_{\mathrm{R}}}{L}\frac{\partial A}{\partial t} = \left[-\alpha_1 - i\delta - i\frac{\beta_{2,\mathrm{FF}}}{2}\frac{\partial^2}{\partial\tau^2}\right]A$$

$$+ \left[i\gamma_1|A|^2 + 2i\gamma_{12}|B|^2\right]A + i\kappa BA^* + S, \quad (3)$$

$$\frac{t_{\mathrm{R}}}{L}\frac{\partial B}{\partial t} = \left[-\alpha_2 - 2i\delta - \Delta\beta_1\frac{\partial}{\partial\tau} - i\frac{\beta_{2,\mathrm{SH}}}{2}\frac{\partial^2}{\partial\tau^2}\right]B$$

$$+ \left[i\gamma_2|B|^2 + 2i\gamma_{21}|A|^2\right]B + i\kappa^*A^2, \quad (4)$$

where A and B are the FF and SH field envelopes in units of $\sqrt{\mathrm{W}}$, S is the CW driving field, $\alpha_{1,2}$ are the optical losses, t_{R} is the round trip time, L is the total cavity length, δ is the phase detuning between the optical source and the closest cavity resonance, $\Delta\beta_1$ is the walk-off, $\gamma_{1,2}$ are the self-phase modulation (SPM) coefficients, $\gamma_{12,21}$ are the cross-phase modulation (XPM) coefficients, and κ is the SHG contribution defined in equation (1). We adopt a two-time scales description, where the *fast time* τ governs the intra-cavity field evolution, while the *slow time* t describes the evolution of the system over time scales larger than t_{R}. Its definition relies on the Ikeda map approximation [53]:

$$t_{\mathrm{R}}\frac{\partial A(t = nt_{\mathrm{R}}, \tau)}{\partial t} = A_{n+1}(z=0,\tau) - A_n(z=0,\tau). \quad (5)$$

The use of the full dispersion profile [54], computed and discussed in the previous section, is implemented in a well known split-step algorithm [49] in the Fourier domain. For further details on the numerical implementation, we address the reader to Appendix.

The Kerr SPM and XPM coefficients have been estimated from the transverse mode profiles through [55]:

$$\gamma_{\mathrm{m,n}} = \frac{n_2\omega}{c}Q_{\mathrm{m,n}}, \quad (6)$$

with the overlap integral $Q_{\mathrm{m,n}}$ defined as [34, 56]:

$$Q_{\mathrm{m,n}} = \frac{\int_{\Omega}|\mathbf{e}_{\mathrm{t,m}}|^2|\mathbf{e}_{\mathrm{t,n}}|^2\mathrm{d}\mathbf{\Omega}}{\int_{\Omega}|\mathbf{e}_{\mathrm{t,m}}|^2\mathrm{d}\mathbf{\Omega}\int_{\Omega}|\mathbf{e}_{\mathrm{t,n}}|^2\mathrm{d}\mathbf{\Omega}}. \quad (7)$$

Here, $\mathbf{e}_{\mathrm{t,1}}$ and $\mathbf{e}_{\mathrm{t,2}}$ are the profiles of the transverse interacting modes, $\mathbf{\Omega}$ the waveguide cross-section, $n_2 = 26 \times 10^{-18}$ m^{2}W^{-1} [17] the nonlinear refractive index of AlGaAs, whose dispersion is neglected for simplicity (i.e. n_2 is considered constant in the whole spectral domain). We computed the Kerr coefficients (γ_1, γ_2, γ_{12}, γ_{21}) = (732, 1716, 499, 732) m^{-1}W^{-1}.

From our previous discussion, the SHG efficiency κ has a spatial dependence $\kappa = \kappa(\theta)$. In the dynamical simulation, this results in a fast time dependence $\kappa = \kappa(\tau)$, which we will take into account to properly embed the $\bar{4}$-QPM ring configuration.

We next show the simulations results considering an input power $P_{\mathrm{in}} = 100$ mW and optical losses $\alpha_1 = 10$ dB/cm, $\alpha_2 = 20$ dB/cm.

3.2 Simulation results

To simulate the OFC generation dynamics from the coupled equations (3) and (4), we spectrally sweep a cavity resonance around the driving wavelength $\lambda \simeq 1550$ nm. This procedure, which mimics the experimental comb excitation, is shown in Figure 3a. We start the simulation in a blue detuned regime, i.e. by pumping the system at wavelengths λ_{P} slightly smaller than a given reference resonance λ_0 ($\lambda_{\mathrm{P}} < \lambda_0$), then we linearly increase δ until we reach a red-detuned regime $\lambda_{\mathrm{P}} > \lambda_0$. At this point λ_{P}, and consequently δ, are kept constant to verify the stability of the excited OFC regime.

Figure 3b shows the energy stored in the cavity versus the total number of round trips, in the different energy scales associated with waves A (E_A) and B (E_B). These are computed as the fast-time integral of the intra-cavity intensities $|A|^2$ and $|B|^2$:

$$E_A = \int_{-t_{\mathrm{R}}/2}^{t_{\mathrm{R}}/2}|A|^2\mathrm{d}\tau. \quad (8)$$

These two quantities differ by about three orders of magnitude, being most of the power carried in the spectral domain around the driving wavelength λ_0. Nonetheless, we can notice an important energy build-up of the FF wave while δ increases and we approach the resonance condition. Above a certain power threshold, a chaotic transition clearly arises and, accordingly, we observe a chaotic nonlinear coupling to the SH domain. Finally, the emergence of a step indicates the likely excitation of a CS regime.

To sustain these statements and fully describe the comb generation, Figure 3 shows four different snapshots of the intra-cavity field (Figs. 3d, 3f, 3h, 3j) and their corresponding spectra (Figs. 3c, 3e, 3g, 3i). In Figures 3c and 3d, the system is in a blue-detuned regime but close to a resonance condition ($\lambda_{\mathrm{P}} - \lambda_0 = -34$ pm). We observe a parametric oscillation which couples efficiently the two spectral domain $\omega_0 \leftrightarrows 2\omega_0$. In Figure 3d, we can observe how the two waves have opposite phases. As the detuning increases and bandwidth broadens, the phase drift between the periodic patterns at ω_0 and $2\omega_0$ can be read as a signature of the non-zero walk-off which is detrimental to synchronize the dynamical evolution in the two separate spectral domains. Notably, typical SH powers are at a mW level, while the FF wave is three orders of magnitude more powerful (~ 1 W), and the same conclusion can be drawn for the other reported OFC regimes. Increasing the detuning ($\lambda_{\mathrm{P}} - \lambda_0 = 86$ pm), we can observe, in Figures 3e and 3f, a MI regime and the associated primary comb. The FF wave dominates the resulting dynamics, as the envelope A forms a periodic pattern while B is slaved to it. In the chaotic regime ($\lambda_{\mathrm{P}} - \lambda_0 = 170$ pm, Figs. 3g and 3h), similarly, most of the power is carried by the FF wave and is chaotically coupled to the SH domain. Finally, Figures 3i and 3j show the final excited comb state (for a detuning $\lambda_{\mathrm{P}} - \lambda_0 = 860$ pm). This consists of a single FF cavity soliton which, due to efficient SHG, couples part of the intracavity power around the SH. Thus the resulting dynamics consists of a single CS confined around the FF and coupled to a dispersive wave at SH. The anomalous
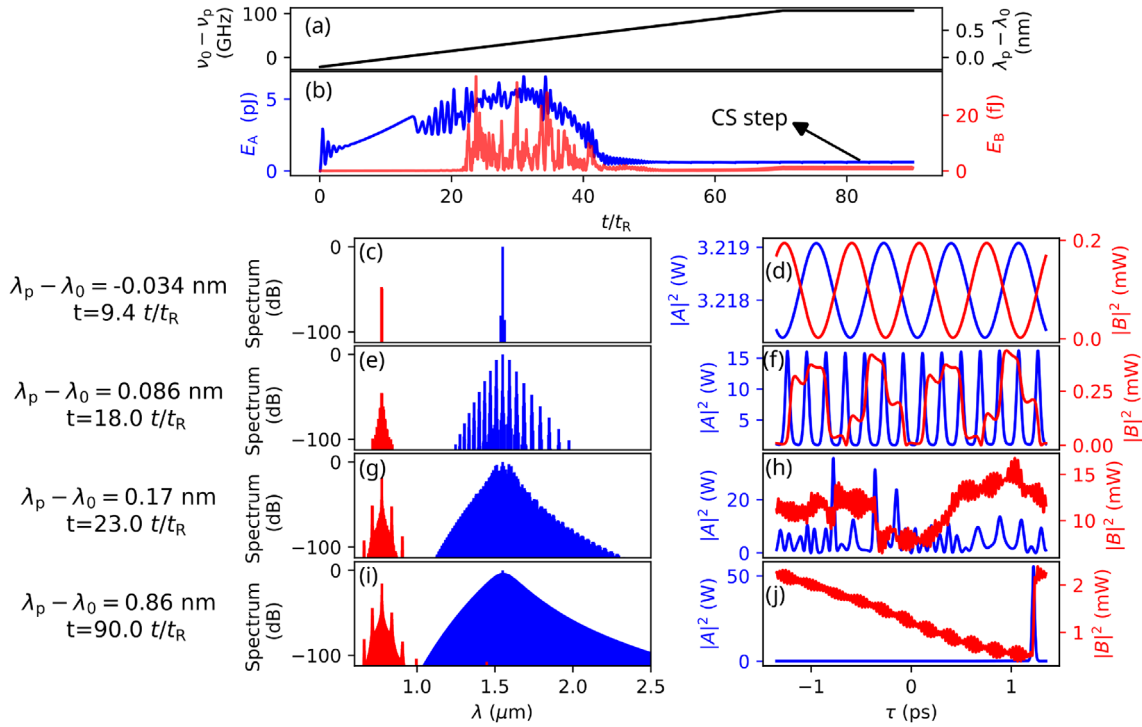
Figure 3. Optical frequency comb generation dynamics. In (a) we report the laser cavity detuning, while in (b) the intra-cavity energy of the FF (blue) and SH (red) fields. In the bottom part of the figure, we report the snapshots for different spectral (c,e,g,i) and temporal (d, f, h, j) OFC regimes: (c, d) OPO, (e, f) modulation instability, (g, h) chaos and (i, j) a FF CS coupled to a SH dispersive wave.

dispersion around ω_0 ($\beta_{2,\mathrm{FF}} < 0$) sustains the soliton propagation. On the other hand, normal dispersion at $2\omega_0$ ($\beta_{2,\mathrm{SH}} > 0$) does not allow for temporal confinement of the spectral components in the SH domain. As a consequence, all the power converted at $2\omega_0$ by the FF CS is rapidly dispersed by the system.

Therefore, the generation of bicolor CSs [12] in the AlGaAs-on-insulator (AlGaAs-OI) platform at telecom wavelengths is intrinsically limited by the normal dispersion profile at shorter wavelengths (i.e. around $2\omega_0$). This is a direct consequence of the absorption peak close to the SH wavelength $\lambda_{\mathrm{SH}} = 0.775$ μm. Notably, a pumping scheme $\lambda_{\mathrm{P}} \sim 1.95$ μm for a SHG assisted supercontinuum generation has been recently proposed [57]. In this specific case, supposing that a phase matching condition for the process $\omega_0 \leftrightarrows 2\omega_0$ is satisfied, the dispersion profile is optimal at both ω_0 and $2\omega_0$, see Figure 2f. As a consequence, the generation of bicolor CSs is not just possible, but it also represents a strong dynamical attractor.

In a telecom pumping scheme, a suitable solution consists in engineering the chromatic dispersion, for instance by a proper longitudinal modification of the waveguide profile [40, 41], which introduces local mirroring effects and frequency splittings that are exploitable for dispersion management. Recently, some prototypes of rings [42, 58] or Fabry-Perot [59, 60] resonators of this sort have been reported.

An alternative approach could involve decoupling the nonlinear problem $\chi^{(2)} + \chi^{(2)}$, by designing two separate photonic devices, which should be eventually integrated in a single circuit. An example can be a pure Kerr microring with a SHG optical feedback. With this solution in mind, let us proceed to describe an optimal AlGaAs waveguide design for efficient frequency doubling.

4 U-shaped AlGaAs waveguide design for efficient frequency doubling

If we aim at narrow-band SHG without caring about dispersive effects, we can target the PM condition between the TE_{00} and TM_{00} modes [22] with no further constraints on the waveguide cross-section. This approach enhances the nonlinear process thanks to the larger overlap integral between fundamental modes. This process can be generalized by letting the waveguide turn and be wrapped in a snaky fashion [47]. The scheme of the problem is depicted in Figure 4a, where we show a U-shaped waveguide with a TE_{00} mode excited at $\lambda_0 = 1.55$ μm and phase-matched to the TM_{00} mode at its SH. The design must optimize SHG all along the waveguide. For this reason, the waveguide width w_0 in the straight section differs from the width w_1 of the curved section, so as to preserve the modal-PM and $\bar{4}$-QPM conditions, respectively. Specifically, type-I modal PM arises whenever the difference of the effective indices Δn_{eff} corresponding to the interacting modes is null, i.e. $\Delta n_{\mathrm{eff}} = 0$. In a curved section, the
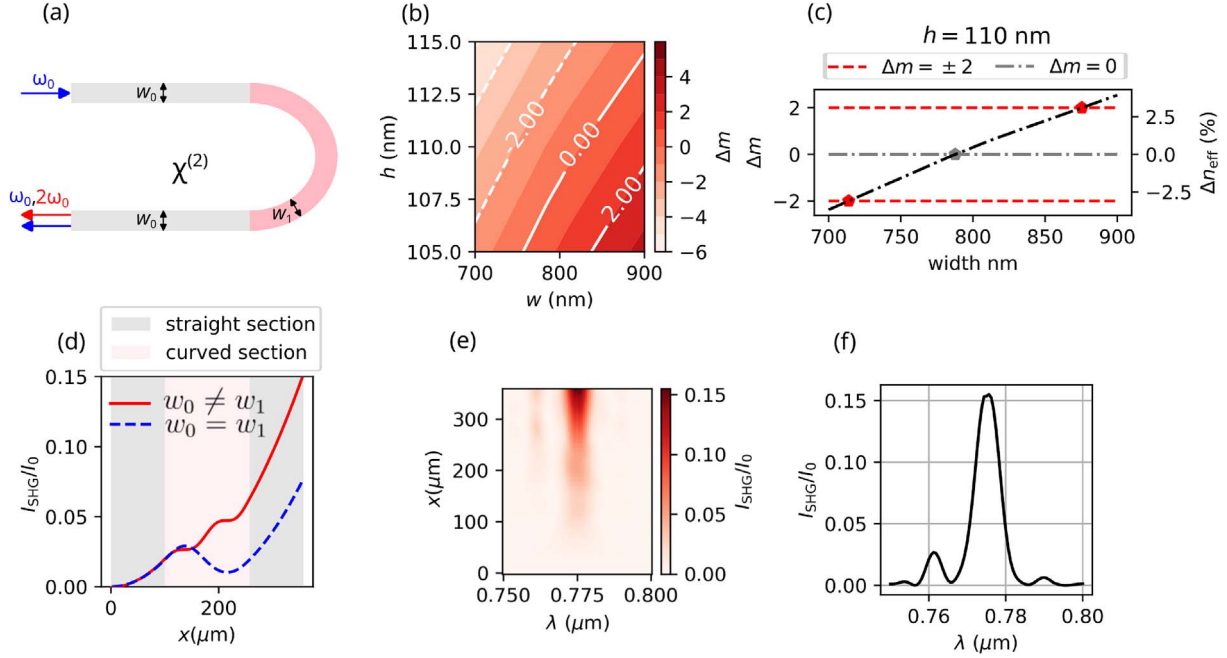
Figure 4. (a) Scheme of U-shape waveguide design for frequency doubling. (b) Color map of the azimuthal number difference Δm between the TE_{00} mode at ω_0 and the TM_{00} mode at $2\omega_0$. (c) Δm vs the waveguide width for height $h = 110$ nm. Modal PM and $\bar{4}$-QPM conditions are reported in red and gray dashed line, respectively, while the markers correspond to PM. (d) Fraction of the power converted from FF to SH. The red line refers to the optimal situation where a change of the waveguide width enables to fulfill the $\bar{4}$-QPM condition in the curved section. The blue dashed line considers a constant width through the whole trajectory. (e) Spectral evolution of I_{SHG}. (f) Asymmetric SHG spectrum of a U-shaped $\chi^{(2)}$ waveguide.

condition for PM takes into account the difference between the azimuthal orders, i.e. $\Delta m = 2m_{FF} - m_{SH} = \pm 2$.

From the map of Δm vs. h and w reported in Figure 4b, we can see that typical waveguide sections for phase matching between TE_{00} (ω) and TM_{00} (2ω) modes are much shallower than those considered above for $h = 400$ nm. Specifically, we note a more pronounced aspect ratio which tends to a quite-planar waveguide ($h \ll w$). The resulting guided modes have typically steep dispersion profiles which are hardly manageable in a broadband domain.

Let us now set, for convenience, $h = 110$ nm. The resulting Δm vs. w diagram is reported in Figure 4c, which shows the $\bar{4}$-QPM and MPM conditions. The intersection with the black dashed line determines the corresponding PM widths for w_0 and w_1. Interestingly, they differ by about hundreds nm, which means that changing the waveguide width in the straight-to-curved section transition may significantly improve the SH conversion.

In order to show that, let us calculate the SHG intensity I_{SHG} under the undepleted-pump approximation. We suppose two straight arms of 100 µm connected by an arc of radius $R = 50$ µm. Figure 4d shows the two cases: I) both the modal PM and $\bar{4}$-QPM conditions are respected in the straight and the curved section, respectively (with phase matched widths $w_0 \neq w_1$); II) the modal-PM condition is satisfied in the two straight sections, but the $\bar{4}$-QPM condition is not fulfilled in the arc section and the width is kept constant ($w_0 = w_1$). To take into account

the dependence of κ on Δm, namely $\kappa = \kappa(\Delta m)$, we calculate the resulting accumulated phase ϕ between the interacting modes TE_{00} (ω) and TM_{00} (2ω) along the propagation trajectory in equation (1), i.e. $\kappa = \kappa(\phi(\Delta m))$. In the plot we show the fraction of converted power I_{SHG}/I_0, being I_0 the driving field intensity, as a function of the propagation length x. We can see that the parabolic trend of the SH intensity buildup is preserved in the straight arms for the two cases, since the modal PM condition is fulfilled. In the curved section, the typical QPM trend occurs for case I [61], while I_{SHG}/I_0 goes down for case II (phase mismatch).

Interestingly, in the ideal case where PM is satisfied all along a U-shaped lossless waveguide, the net power conversion is ~16% for a total propagation length of just ~300 µm. It is worth mentioning that, in the seek of maximizing the SHG efficiency, it is crucial to consider realistic pump depletion and optical losses, here neglected for simplicity. While this will be dealt with in future work, for the moment we may clearly state that AlGaAs may lead to an efficient $\omega_0 \rightarrow 2\omega_0$ on-chip conversion in an integrated circuit with minimal propagation length.

4.1 SHG spectral symmetry breaking

Besides the monochromatic frequency conversion $\omega_0 \rightarrow 2\omega_0$, if we aim to integrate the $\chi^{(2)}$ U-shaped waveguide in a compact $\chi^{(2)} + \chi^{(3)}$ device, it is important to

estimate the spectral dependence of the frequency doubling process. This can be done if we calculate the chromatic dependence of the total accumulated phase between the interacting modes TE_{00} and TM_{00}, all along the propagation trajectory. The resulting expression for the SHG efficiency of equation (1) now takes the form $\kappa = \kappa(\phi(\Delta m, \lambda))$. Notably, the dependence of the accumulated phase $\phi(\Delta m, \lambda)$ on Δm and λ differs between the straight and the curved sections, given that Δm has a strict waveguide width dependence (namely, $\Delta m = \Delta m(w)$). In what follows we compute the spectral dependence of the U-shaped design, phase-matched in both the straight and curved section.

The results of these calculations, reported in Figures 4e and 4f, are again performed under the undepleted-pump approximation. In Figure 4e, we report the 3D color map of the total intensity I_{SHG} converted around the SH vs the propagation length x and the wavelength λ, normalized to the driving field intensity I_0. The spectrum of $I_{SHG}(x, \lambda)$ is clearly peaked at the SH wavelength $\lambda_0/2$, for which the constructive power build-up is guaranteed by the design, all along the U-shaped waveguide. On the contrary, we have not expressly optimized the conversion for the adjacent wavelengths, since it could possibly attenuate the conversion at $\lambda_0/2$. The resulting SH narrow-band power build-up exhibits an unclear behavior which is not necessarily constructive in the whole spectral domain and along the whole waveguide length. Moreover, a spectral asymmetry is evident with respect to the typical $sinc^2$ shape [61]. This is even more evident in the plot of the final I_{SHG} in Figure 4f. Here the $sinc^2$ symmetry breaking is due to the fact that, to preserve a constructive power build-up at $\lambda_0/2$, we change the waveguide width $w_0 \to w_1$ while switching from the straight to the curved section. This responds to the quest of fulfilling both the MPM and $\bar{4}$-QPM conditions, respectively. While doing that, we span Δm over the narrow-band SHG spectrum, spanning also over different partially constructive interference conditions. As a result, the symmetry of the $sinc^2$ SH generated intensity, resulting from a straight propagation through a $\chi^{(2)}$ phase-matched waveguide, is broken in a U-shaped geometry where PM is granted all along the waveguide at $\lambda_0/2$.

In perspective, it is interesting to note how a wrapped snaking waveguide, composed by different U-shaped sections optimized for different SHG wavelengths, could be designed to optimize a broad-band or comb-like SHG spectrum.

5 Fabrication process

The technology we have developed to fabricate AlGaAs-OI waveguides [62] is based on adhesive bonding [17, 63] between a GaAs substrate, with the desired epitaxy of AlGaAs on top, and a thermally oxidized Si carrier wafer (see Figs. 5a–5d, for the entire process).

In Figure 5a, we schematize the bonding process. The AlGaAs epitaxy is grown by molecular beam epitaxy (MBE) on a (100) GaAs substrate and it consists of two layers: an active $Al_{0.18}Ga_{0.82}As$ membrane (400 or 110 nm, depending on the design) and a sacrificial

$Al_{0.8}Ga_{0.2}As$ etch-stop layer. A SiO_2 layer is then deposited on the AlGaAs wafer to improve adhesion in the following bonding process. A thin benzocyclobutene (BCB) layer is spin coated on the thermal SiO_2 (2 μm) of the Si carrier, and then the AlGaAs wafer is back-flipped on it. The bonding is carried out by applying pressure and heat.

The 350 μm-thick GaAs substrate is removed in two steps using a citric acid/hydrogen peroxide solution (volume ratio 5:1): the first one at 60 °C to rapidly remove most of the substrate, the second one at 20 °C to remove the last 50 μm at a slower etch rate to minimize the tolerances due to the etching process. The sample is then rinsed in deionized water and quickly cleaned with HCl [22]. The etch-stop layer is removed using a buffered oxide solution (BOE 7:1). The result of this process is sketched on Figure 5b.

After the substrate removal, a thin SiO_2 protective layer is deposited on the $Al_{0.18}Ga_{0.18}As$ membrane. The e-beam lithography (EBL) is carried out using hydrogen silsesquioxane (HSQ) resist (Fig. 5c). Finally, the patterns are transferred to the semiconductor membrane by ICP-RIE using a $SiCl_4$/Ar gas mixture (Fig. 5d).

With this process we fabricated optical waveguides and ring resonators (Figs. 5e and 5f). In Figure 5e, we show a set of micro-rings with a radius $R = 50$ μm with bus waveguides wrapping around to optimize the evanescent coupling. In Figure 5f, we show four scanning electron microscope (SEM) pictures: two narrow coupled waveguides (top left), PhC waveguides for dispersion management [40] (top right), a waveguide facet (bottom left) and sub-wavelength (SW) grating couplers [64] (bottom right).

5.1 Experimental characterization

The nonlinear characterization of the structures described in this paper is currently in progress and it will be the object of future work. In Figures 5g and 5h we report a preliminary linear characterization of a ring resonator. The particular bell shape of the transmission spectrum (Fig. 5g) is due to SW grating couplers used to inject and to extract light into/from the chip. We notice a good extinction ratio, which indicates the vicinity to the critical coupling condition. We estimated quality factors of around $\sim 10^5$. We measured a group index (Fig. 5h) consistent with the designed dispersion profile. The associated group velocity dispersion $\beta_2 \sim -2.5$ ps^2/m around the pump wavelength confirms the prescribed anomalous dispersion regime, suitable for solitons generation.

6 Conclusion and perspectives

While OFCs are deeply studied in either purely quadratic [1–3, 32] or Kerr [4, 5, 7, 17, 18, 50, 53] systems, only recently mixed $\chi^{(2)} + \chi^{(3)}$ nonlinear passive resonators have been conceptualized and demonstrated [10–12, 30, 37, 38], thanks to key technological advances leading to the possibility of efficient nonlinear micro-photonics integration [55, 65]. In this work, we have proposed and discussed the perspective impact of AlGaAs for $\chi^{(2)} + \chi^{(3)}$ nonlinear
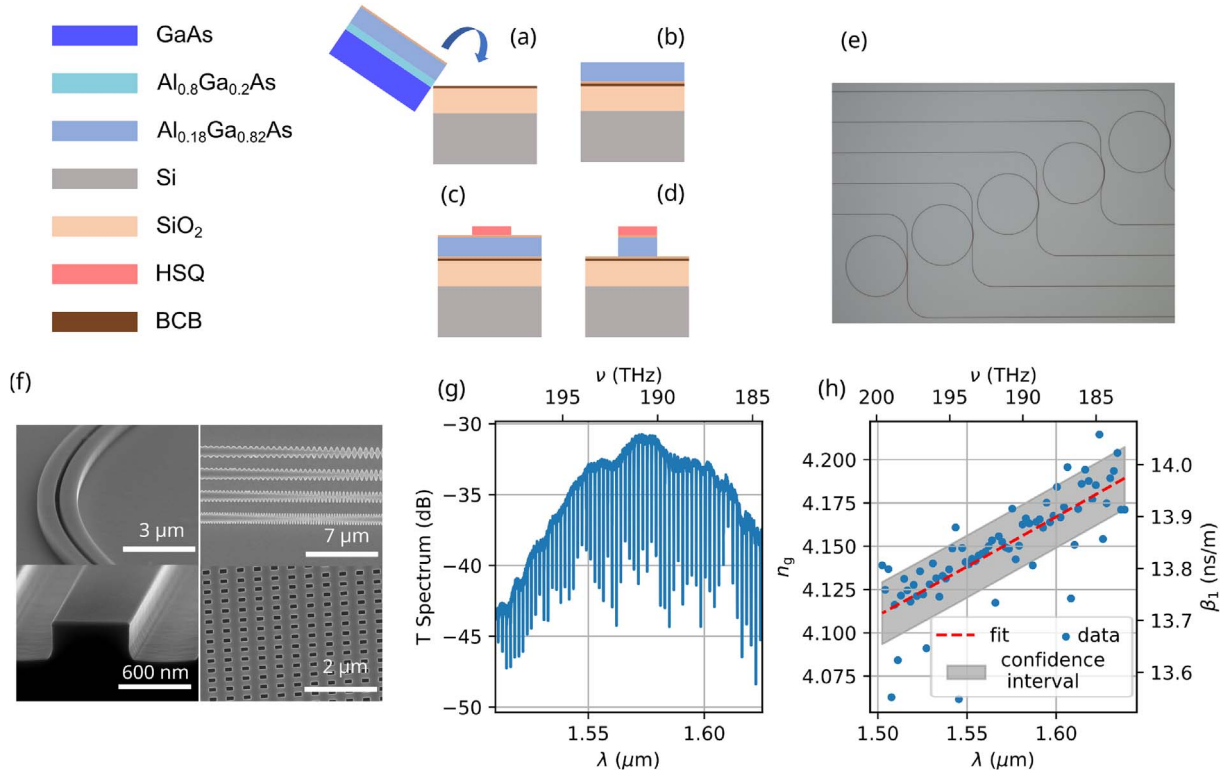
Figure 5. (a–d) Fabrication process: (a) adhesive bonding of the AlGaAs epitaxy on a silicon substrate; (b) GaAs substrate removal; (c) HSQ resist spun and patterned by electron beam lithography; (d) ICP RIE etching; (e) Ring resonators and bus waveguides; (f) SEM pictures of fabricated devices: (top left) bus waveguide and ring resonator in the evanescent coupling region; (top right) fabrication test of longitudinal corrugated PhC waveguides for dispersion engineering; (bottom left) waveguide end facet; (bottom right) SW grating coupler. (g) Optical transmission of a ring resonator and (h) its associated group index n_g, calculated for each resonances (blue scatters) and fitted in function of λ (red dashed line).

photonics at the telecom wavelengths. We found that Kerr-like cavity solitons can be formed and coupled to dispersive waves at SH, which tends to disperse most of the SH power. For broadband SHG applications, this represents a detrimental effect that is due to steep and hardly manageable dispersion profiles at $2\omega_0$. Dispersion engineering [41, 42, 44, 58, 59] and inverse design [40, 43] approaches represent a valid perspective solution and it is currently under investigation.

A possible alternative is decoupling the $\chi^{(2)} + \chi^{(3)}$ nonlinear problem and to design a Kerr nonlinear resonator with a purely quadratic SHG optical feedback. We have presented a U-shaped $\chi^{(2)}$ design which is capable of about $\sim 16\%$ $\omega_0 \to 2\omega_0$ conversion with a minimal propagation length (~ 300 μm).

Interestingly, we have predicted a spectral symmetry breaking due to the spanning over different phase matching conditions, in a U-shaped or snaking waveguide geometries. Notably, symmetry breaking is a key concept in physics: besides being the basic mechanism for energy-to-mass conversion in Gauge theory [66], in the field of optics it is of crucial importance for spin glasses [67] or random lasers [68]. For Kerr mediums, a symmetry-breaking transition can be responsible of periodic pattern generation [69], and in the context of nonlinear passive resonators it can generate a trapping potential for CSs [70]. Eventually, symmetry

can be recovered by a chirped pulse pump [8]. As a perspective, one can investigate the possibility of designing spectral potential traps, as well as broadband SHG integrated photonics.

Conflicts of interest

The authors declare no conflicts of interest.

Data availability statement

Data underlying the results presented in this paper are not publicly available but may be obtained from the authors upon reasonable request.

Author contribution statement

FR Talenti: conceptualization, theoretical modelling and simulations, design, experiments, writing; L Lovisolo: development of the technology, fabrication, design, experiments, writing; A Gerini: design, fabrication, writing; H Peng: conceptualization; P Parra-Rivas, T Hansson, Y Sun: theory and simulations; C Alonso-Ramos: fabrication and development of the technology; M Morassi, A Lemaître: AlGaAs epitaxial growth; A Harouri: wafer bonding; C Koos: project administration, funding acquisition, supervision; S Wabnitz: theory, project administration, funding acquisition, supervision, writing; L Vivien: conceptualization, development of the technology, fabrication, supervision; G Leo: project administration, funding acquisition, supervision, writing.

References

1 Ulvila V, Phillips CR, Halonen L, Vainio M, Frequency comb generation by a continuous-wave-pumped optical parametric oscillator based on cascading quadratic nonlinearities, *Opt. Lett.* **38**, 4281 (2013). https://doi.org/10.1364/ol.38.004281.

2 Ricciardi I, et al. Frequency comb generation in quadratic nonlinear media, *Phys. Rev. A.* **91**, 063839 (2015). https://doi.org/10.1103/physreva.91.063839.

3 Leo F, et al., Walk-off-induced modulation instability, temporal pattern formation, and frequency comb generation in cavity-enhanced second-harmonic generation, *Phys. Rev. Lett.* **116**, 033901 (2016). https://doi.org/10.1103/physrevlett.116.033901.

4 Del'Haye P, Herr T, Gavartin E, Gorodetsky ML, Holzwarth R, Kippenberg TJ, Octave spanning tunable frequency comb from a microresonator, *Phys. Rev. Lett.* **107**, 063901 (2011). https://doi.org/10.1103/physrevlett.107.063901.

5 Herr T, et al., Temporal solitons in optical microresonators, *Nat. Photonics.* **8**, 145 (2013). https://doi.org/10.1038/nphoton.2013.343.

6 Wabnitz S, Suppression of interactions in a phase-locked soliton optical memory, *Opt. Lett.* **18**, 601 (1993). https://doi.org/10.1364/ol.18.000601.

7 Rowley M, et al., Self-emergence of robust solitons in a microcavity, *Nature* **608**, 303 (2022). https://doi.org/10.1038/s41586-022-04957-x.

8 Talenti FR, Sun Y, Parra-Rivas P, Hansson T, Wabnitz S, Control and stabilization of Kerr cavity solitons and breathers driven by chirped optical pulses, *Opt. Commun.* **546**, 129773 (2023). https://doi.org/10.1016/j.optcom.2023.129773.

9 Szabados J, Sturman B, Breunig I, Frequency comb generation threshold via second-harmonic excitation in $\chi^{(2)}$ optical microresonators, *APL Photonics* **5**, 116102 (2020). https://doi.org/10.1063/5.0021424.

10 Bruch AW, Liu X, Surya JB, Zou CL, Tang HX, On-chip $\chi^{(2)}$ microring optical parametric oscillator, *Optica* **6**, 1361 (2019). https://doi.org/10.1364/optica.6.001361.

11 Bruch AW, et al., Pockels soliton microcomb, *Nat. Photonics* **15**, 21 (2020). https://doi.org/10.1038/s41566-020-00704-8.

12 Lu J, et al., Two-colour dissipative solitons and breathers in microresonator second-harmonic generation, *Nat. Commun.* **14**, 2798 (2023). https://doi.org/10.1038/s41467-023-38412-w.

13 Coudrat L, Boulliard G, Gérard JM, Lemaître A, Degiron A, Leo G, Unravelling the nonlinear generation of designer vortices with dielectric metasurfaces, *Light Sci. Appl.* **14**, 51 (2025). https://doi.org/10.1038/s41377-025-01741-0.

14 de Ceglia D, et al., Nonlinear spin-orbit coupling in optical thin films, *Nat. Commun.* **15**, 1625 (2024). https://doi.org/10.1038/s41467-024-45607-2.

15 Chopin A, et al., Ultra-efficient generation of time-energy entangled photon pairs in an InGaP photonic crystal cavity, *Commun. Phys.* **6**, 77 (2023). https://doi.org/10.1038/s42005-023-01189-x.

16 Schuhmann J, et al., Hybrid III-V/silicon quantum photonic device generating broadband entangled photon pairs, *PRX Quantum.* **5**, 040321 (2024). https://doi.org/10.1103/prxquantum.5.040321.

17 Pu M, Ottaviano L, Semenova E, Yvind K, Efficient frequency comb generation in AlGaAs-on-insulator, *Optica.* **3**, 823 (2016). https://doi.org/10.1364/optica.3.000823.

18 Chang L, et al., Ultra-efficient frequency comb generation in AlGaAs-on-insulator microresonators, *Nat. Commun.* **11**, 1331 (2020). https://doi.org/10.1038/s41467-020-15005-5.

19 Marty G, Combrié S, Raineri F, De Rossi A, Photonic crystal optical parametric oscillator, *Nat. Photonics.* **15**, 53 (2020). https://doi.org/10.1038/s41566-020-00737-z.

20 Chopin A, et al., Canonical resonant four-wave-mixing in photonic crystal cavities: tuning, tolerances and scaling, *IEEE J. Sel. Top. Quantum Electron.* **29**, 5100913 (2022). https://doi.org/10.1109/jstqe.2022.3229164.

21 Chang L, et al., Strong frequency conversion in heterogeneously integrated GaAs resonators, *APL Photonics* **4**, 036103 (2019). https://doi.org/10.1063/1.5065533.

22 Stanton EJ, et al., Efficient second harmonic generation in nanopho tonic GaAs-on-insulator waveguides, *Opt. Express.* **28**, 9521 (2020). https://doi.org/10.1364/oe.389423.

23 Gerini A, et al., Second harmonic generation in monolithic GaAs shallow waveguides, *Opt. Express* **33**, 17560 (2025). https://doi.org/10.1364/OE.540737.

24 Poulvellarie N, et al., Second-harmonic generation enabled by longitudinal electric-field components in photonic wire waveguides, *Phys. Rev. A.* **102**, 023521 (2020). https://doi.org/10.1103/physreva.102.023521.

25 Ciret C, et al., Influence of longitudinal mode components on second harmonic generation in III-V-on-insulator nanowires, *Opt. Express* **28**, 31584 (2020). https://doi.org/10.1364/oe.402150.

26 Poulvellarie N, et al., Efficient type II second harmonic generation in an indium gallium phosphide on insulator wire waveguide aligned with a crystallographic axis, *Opt. Lett.* **46**, 1490 (2021). https://doi.org/10.1364/ol.418064.

27 Pantzas K, et al., Continuous-wave second-harmonic generation in orientation-patterned gallium phosphide waveguides at telecom wavelengths, *ACS Photonics* **9**, 2032 (2022). https://doi.org/10.1021/acsphotonics.2c00156.

28 Akin J, Zhao Y, Misra Y, Haque AKMN, Fang K, InGaP $\chi^{(2)}$ integrated photonics platform for broadband, ultra-efficient nonlinear conversion and entangled photon generation, *Light Sci. Appl.* **13**, 290 (2024). https://doi.org/10.1038/s41377-024-01653-5.

29 Gerini A, et al., Electrically injected InGaAsP/AlGaAs optical parametric oscillator: design and technology, *J. Opt. Soc. Am. B.* **38**, B40 (2021). https://doi.org/10.1364/josab. 425018.

30 Talenti FR, et al., Frequency comb generation dynamics in $\chi^{(2)} + \chi^{(3)}$ AlGaAs microresonators, *EPJ Web Conf.* **309**, 08003 (2024). https://doi.org/10.1051/epjconf/20243090 8003.

31 Talenti FR, et al., Bistable soliton optical frequency combs in a second-harmonic generation Kerr cavity, *Opt. Lett.* **50**, 2037 (2025). https://doi.org/10.1364/OL.551383.

32 Hansson T, Parra-Rivas P, Bernard M, Leo F, Gelens L, Wabnitz S, Quadratic soliton combs in doubly resonant second-harmonic generation, *Opt. Lett.* **43**, 6033 (2018). https://doi.org/10.1364/ol.43.006033.

33 Leo F, et al., Frequency-comb formation in doubly resonant second-harmonic generation, *Phys. Rev. A.* **93**, 043831 (2016). https://doi.org/10.1103/physreva.93.043831.

34 Hansson T, Parra-Rivas P, Wabnitz S, Modeling of dual frequency combs and bistable solitons in third-harmonic generation, *Commun. Phys.* **6**, 59 (2023). https://doi.org/10.1038/s42005-023-01176-2.

35 Trillo S, Wabnitz S, Nonlinear parametric mixing instabilities induced by self-phase and cross-phase modulation, *Opt. Lett.* **17**, 1572 (1992). https://doi.org/10.1364/ol.17.001572.

36 Buryak AV, Trillo S, Kivshar YS, Optical solitons supported by competing nonlinearities, *Opt. Lett.* **20**, 1961 (1995). https://doi.org/10.1364/ol.20.001961.

37 Villois A, Kondratiev N, Breunig I, Puzyrev DN, Skryabin DV, Frequency combs in a microring optical parametric oscillator, *Opt. Lett.* **44**, 4443 (2019). https://doi.org/10.1364/ol.44.004443.

38 Xue X, et al., Second-harmonic-assisted four-wave mixing in chip-based microresonator frequency comb generation, *Light Sci. Appl.* **6**, e16253 (2016). https://doi.org/10.1038/lsa.2016.253.

39 Phillips CR, Jankowski M, Flemens N, Fejer MM, General framework for ultrafast nonlinear photonics: unifying single and multi-envelope treatments, *Opt. Express.* **32**, 8284 (2024). https://doi.org/10.1364/oe.513856.

40 Talenti FR, Wabnitz S, Ghorbel I, Combrié S, Aimone-Giggio L, De Rossi A, Fast dispersion tailoring of multimode photonic crystal resonators, *Phys. Rev. A.* **106**, 023505 (2022). https://doi.org/10.1103/physreva.106.023505.

41 De Rossi A, Combrié S, The dawn of chimera optical resonators, *Nat. Photonics* **18**, 112 (2024). https://doi.org/10.1038/s41566-023-01376-w.

42 Moille G, Lu X, Stone J, Westly D, Srinivasan K, Fourier synthesis dispersion engineering of photonic crystal microrings for broadband frequency combs, *Commun. Phys.* **6**, 144 (2023). https://doi.org/10.1038/s42005-023-01253-6.

43 Gray D, West GN, Ram RJ, Inverse design for waveguide dispersion with a differentiable mode solver, *Optics Express.* **32**, 30541 (2024). https://doi.org/10.1364/oe.530479.

44 Lucas E, Yu SP, Briles TC, Carlson DR, Papp SB, Tailoring microcombs with inverse-designed, metadispersion microresonators, *Nat. Photonics* **17**, 943 (2023). https://doi.org/10.1038/s41566-023-01252-7.

45 Abolghasem P, Han JB, Kang D, Bijlani BJ, Helmy AS, Monolithic photonics using second-order optical nonlinearities in multilayer-core Bragg reflection waveguides, *IEEE J. Sel. Top. Quantum Electron.* **18**, 812 (2011). https://doi.org/10.1109/JSTQE.2011.2135841.

46 Kuo PS, Fang W, Solomon GS, $\bar{4}$-quasi-phase-matched interactions in GaAs microdisk cavities, *Opt. Lett.* **34**, 3580 (2009). https://doi.org/10.1364/ol.34.003580.

47 Morais N, et al., Directionally induced quasi-phase matching in homogeneous AlGaAs waveguides, *Opt. Lett.* **42**, 4287 (2017). https://doi.org/10.1364/ol.42.004287.

48 *Ansys* (Lumerical Inc, 2000). Available at https://www.lumerical.com/.

49 Agrawal GP, *Nonlinear fiber optics* (Springer, Berlin, Heidelberg, 2000).

50 Pasquazi A, et al., Micro-combs: A novel generation of optical sources, *Phys. Rep.* **729**, 1 (2018). https://doi.org/10.1016/j.physrep.2017.08.004.

51 Laegsgaard J, Mode profile dispersion in the generalised nonlinear Schrödinger equation, *Opt. Express.* **15**, 16110 (2007). https://doi.org/10.1364/oe.15.016110.

52 Buryak AV, Trapani PD, Skryabin DV, Trillo S, Optical solitons due to quadratic nonlinearities: from basic physics to futuristic applications, *Phys. Rep.* **370**, 63 (2002). https://doi.org/10.1016/s0370-1573(02)00196-5.

53 Hansson T, Wabnitz S, Dynamics of microresonator frequency comb generation: models and stability, *Nanophotonics.* **5**, 231 (2016). https://doi.org/10.1515/nanoph-2016-0012.

54 Dudley JM, Taylor JR, *Supercontinuum generation in optical fibers* (Cambridge University Press, Cambridge, 2010).

55 Leuthold J, Koos C, Freude W, Nonlinear silicon photonics, *Nat. Photonics.* **4**, 535 (2010). https://doi.org/10.1038/nphoton.2010.185.

56 Lin Q, Painter OJ, Agrawal GP, Nonlinear optical phenomena in silicon waveguides: modeling and applications, *Opt. Express.* **15**, 16604 (2007). https://doi.org/10.1364/oe.15.016604.

57 Nishi H, Sugiyama H, Kanno E, Segawa T, Wada K, Matsuo S, Second-harmonic-wave assisted octave-spanning supercontinuum generation in an AlGaAs-on-insulator waveguide, in: *2024 IEEE Silicon Photonics Conference (SiPhotonics), 15–18 April, Tokyo Bay, Japan* (IEEE, 2024), p. 1. https://doi.org/10.1109/siphotonics60897.2024.10543509.

58 Yu SP, Lucas E, Zang J, Papp SB, A continuum of bright and dark-pulse states in a photonic-crystal resonator, *Nat. Commun.* **13**, 3134 (2022). https://doi.org/10.1038/s41467-022-30774-x.

59 Yu SP, Jung H, Briles TC, Srinivasan K, Papp SB, Photonic-crystal-reflector nanoresonators for kerr-frequency combs, *ACS Photonics* **6**, 2083 (2019). https://doi.org/10.1021/acsphotonics.9b00578.

60 Wildi T, Gaafar MA, Voumard T, Ludwig M, Herr T, Dissipative Kerr solitons in integrated Fabry–Perot microresonators, *Optica* **10**, 650 (2023). https://doi.org/10.1364/optica.480789.

61 Boyd RW, Gaeta AL, Giese E, *Nonlinear optics* (Springer, New York, 2008).

62 Mobini E, Espinosa DHG, Vyas K, Dolgaleva K, AlGaAs nonlinear integrated photonics, *Micromachines* **13**, 991 (2022). https://doi.org/10.3390/mi13070991.

63 May S, Clerici M, Sorel M, Supercontinuum generation in dispersion engineered AlGaAs-on-insulator waveguides, *Sci. Rep.* **11**, 2052 (2021). https://doi.org/10.1038/s41598-021-81555-3.

64 Halir R, et al., Waveguide sub-wavelength structures: a review of principles and applications, *Laser Photonics Rev.* **9**, 25 (2014). https://doi.org/10.1002/lpor.201400083.

65 Vermeulen N, et al., Post-2000 nonlinear optical materials and measurements: data tables and best practices, *J. Phys. Photonics* **5**, 035001 (2023). https://doi.org/10.1088/2515-7647/ac9e2f.

66 Higgs PW, Broken symmetries and the masses of gauge bosons, *Phys. Rev. Lett.* **13**, 508 (1964). https://doi.org/10.1103/physrevlett.13.508.

67 Parisi G, The order parameter for spin glasses: a function on the interval 0–1, *J. Phys A: Math. General.* **13**, 1101 (1980). https://doi.org/10.1088/0305-4470/13/3/042.

68 Massaro LM, et al., Heterogeneous random laser with switching activity visualized by replica symmetry breaking maps, *ACS Photonics* **8**, 376 (2021). https://doi.org/10.1021/acsphotonics.0c01803.

69 Ducci S, Ramazza PL, González-Viñas W, Arecchi FT, Order parameter fragmentation after a symmetry-breaking transition, *Phys Rev Lett.* **83**, 5210 (1999). https://doi.org/10.1103/PhysRevLett.83.5210.

70 Hendry I, et al., Spontaneous symmetry breaking and trapping of temporal Kerr cavity solitons by pulsed or amplitude-modulated driving fields, *Phys. Rev. A.* **97**, 053834 (2018). https://doi.org/10.1103/physreva.97.053834.

71 Butcher JC, A history of Runge-Kutta methods, *Appl. Numer. Math.* **20**, 247 (1996). https://doi.org/10.1016/0168-9274(95)00108-5.

72 Bezanson J, Edelman A, Karpinski S, Shah VB, Julia: A fresh approach to numerical computing, *SIAM Rev.* **59**, 65 (2017). https://doi.org/10.1137/141000671.

Appendix: Numerical implementation

A.1 Normalization

In the numerical implementation of the dynamics of equations (3) and (4), it is important to adapt a proper normalization. In order to minimize the computational cost and to maximize the accuracy, good prescription is that the key parameters and variables assume values close to the unity. In our simulations, we normalized the system according to the following substitutions:

$$
\begin{aligned}
&\alpha_1' = \alpha_1/\alpha_1 = 1, \qquad \alpha_2' = \alpha_2/\alpha_1, \quad \Delta \equiv \delta/\alpha_1, \\
&t' = \alpha_1 L t/t_r, \quad \tau' = \sqrt{\tfrac{2\alpha_1}{|\beta_2|}}\tau, \quad A', B' = \sqrt{\tfrac{\gamma_1}{\alpha_1}}A, B, \\
&\beta_{\mathrm{FF(SH)}}' = \tfrac{\beta_{\mathrm{FF(SH)}}}{\alpha_1}, \quad \beta_{1,\mathrm{FF(SH)}}' = \sqrt{\tfrac{2}{\alpha_1|\beta_{2,\mathrm{FF}}|}}\beta_{1,\mathrm{FF(SH)}}, \\
&\beta_{2,\mathrm{FF(SH)}}' = \beta_{2,\mathrm{FF(SH)}}/|\beta_{2,\mathrm{FF}}| \quad \gamma_1' = \gamma_1/\gamma_1 = 1 \\
&\gamma_{2,12,21}' = \gamma_{2,12,21}/\gamma_1, \quad \kappa' = \sqrt{\tfrac{1}{\gamma_1\alpha_1}}\kappa, \\
&S' = \sqrt{\tfrac{\gamma_1}{\alpha_1^3 L^2}}S,
\end{aligned} \tag{A1}
$$

where we have defined the normalized detuning Δ. The resulting coupled equations are formally identically to the system of equations (3) and (4), except for the prefactor t_{R}/L on the LHS, which vanishes. However, subject to this substitution, the system is dimensionless and typical solutions are of the order ~ 1. It follows that the machine virtual memory used is minimized, and both the CPU efficiency and accuracy are optimized.

A.2 Numerical algorithm

In our simulations we make used of a standard split-step Fourier algorithm [49, 54]. In order to illustrate the procedure, we rewrite the system according to:

$$
\frac{\partial \mathcal{U}}{\partial t} = \mathcal{L}\mathcal{U} + \mathcal{N}\mathcal{U} + \mathcal{S}, \tag{A2}
$$

where the linear $\mathcal{L}$, nonlinear $\mathcal{N}$ and pump $\mathcal{S}$ operators are defined, in normalized units, by comparison with equations (3) and (4):

$$
\mathcal{U} = \begin{pmatrix} A' \\ \mathrm{B}' \end{pmatrix}, \tag{A3}
$$

$$
\mathcal{L}\mathcal{U} = \begin{pmatrix} -\alpha_1' - i\Delta - i\dfrac{\beta_{2,\mathrm{FF}}'}{2}\dfrac{\partial^2}{\partial\tau'^2}, \\[2mm] -\alpha_2' - i2\Delta - \Delta\beta_1'\dfrac{\partial}{\partial\tau'} - i\dfrac{\beta_{2,\mathrm{SH}}'}{2}\dfrac{\partial^2}{\partial\tau'^2} \end{pmatrix}\mathcal{U}, \tag{A4}
$$

$$
\mathcal{N}\mathcal{U} = \begin{pmatrix} \left[i\gamma_1'\left|A'\right|^2 + 2i\gamma_{12}'\left|B'\right|^2\right]A' + i\kappa' B' A'^* \\[2mm] \left[i\gamma_2'|B'|^2 + 2i\gamma_{21}'|A'|^2\right]B' + i\kappa'^* A'^2 \end{pmatrix}, \tag{A5}
$$

$$
\mathcal{S} = \begin{pmatrix} S' \\ 0 \end{pmatrix}. \tag{A6}
$$

The two-steps algorithm works in both the time and Fourier domain in a single discretization step Δt, which connects two consecutive instants t_k and $t_{k+1} = t_k + \Delta t$. The linear block $\partial \mathcal{U}_{\mathrm{L}}/\partial t = \mathcal{L}\mathcal{U} + \mathcal{S}$ is solved analytically in the Fourier domain. The field $\mathcal{U}$ is first transformed to $\tilde{\mathcal{U}}$ by a standard fast Fourier transform (FFT) numerical operator, i.e. $\tilde{\mathcal{U}}(t_k, \omega) \equiv \mathrm{FFT}\{\mathcal{U}(t_k, \tau)\}$. Then, the linear contribution to the evolution of the jth component of the field at the kth step is computed by:

$$
\tilde{\mathcal{U}}_{\mathrm{L},j}(t_{k+1}, \omega) = \tilde{\mathcal{U}}_j(t_k, \omega)e^{\tilde{\mathcal{L}}_j\Delta t} + \frac{\tilde{\mathcal{S}}_j}{\tilde{\mathcal{L}}_j}\left(e^{\tilde{\mathcal{L}}_j\Delta t} - 1\right). \tag{A7}
$$

This expression is valid for the two-field components $j = 1, 2$, and we can note that the second term on the RHS is null for $j = 2$. Next, we transform back $\tilde{\mathcal{U}}_{\mathrm{L},j}(t_{k+1}, \omega)$ to the time domain by means of an inverse fast Fourier transform operation (IFFT), i.e. $\mathcal{U}_{\mathrm{L},j}(t_{k+1}, \tau) = \mathrm{IFFT}(\tilde{\mathcal{U}}_{\mathrm{L},j}(t_{k+1}, \omega))$. At this point, we calculate numerically the nonlinear contribution by means of a 4th order Runge-Kutta solver (RGK4) [71]:

$$
\mathcal{U}_{\mathrm{N},j}(t_{k+1}, \tau) = \mathrm{RGK4}(\mathcal{N}\mathcal{U}_{\mathrm{L},j}(t_{k+1}, \tau)). \tag{A8}
$$

The two-steps (A7) and (A8) are subject to the condition that the linear $\mathcal{L}$ and nonlinear $\mathcal{N}$ operators act separately and independently on the two waves field $\mathcal{U}$. This condition is mathematically fulfilled if and only if their commutator vanishes, i.e. $[\mathcal{L}, \mathcal{N}]\mathcal{U} = 0$ [49]. This is true in the limit $\Delta t \to 0$, and thus the accuracy of procedure crucially relies on the choice of small enough discretization steps Δt.

A.3 Dispersion effects

The contribution of chromatic dispersion effects is evaluated in the Fourier domain and embedded in the linear operator $\tilde{\mathcal{L}}(\omega)$. The system of equations (3) and (4) neglects leading order terms with respect to the GVD. Within this approximation, the operator $\tilde{\mathcal{L}}(\omega)$ reads as:

$$
\tilde{\mathcal{L}}(\omega) \approx \begin{pmatrix} -\alpha_1' - i\Delta + i\beta_{2,\mathrm{FF}}'\omega^2 \\[2mm] -\alpha_2' - 2i\Delta - \Delta\beta_1'\omega + i\beta_{2,\mathrm{SH}}'\omega^2 \end{pmatrix}. \tag{A9}
$$

This approximation is optimal in a narrow band spectral domain, while for broadband dynamics can be detrimental. In our case, we have a doubly resonant system which owns spectral components covering the whole octave spanning FF $\to$ SH domain, with important dispersive effects. For this reason, the use of a full dispersion profile is of crucial importance for the implementation of reliable and realistic models. In multi-envelope systems [39], we can expand

in Taylor series the propagation constant $\beta(\omega)$ (Eq. (2)). The standard substitution reads as [54]:

$$\sum_{k \geq 2}^{\infty} \frac{\beta_k}{k!} \omega^k = \beta(\omega) - \beta_1 \omega - \beta_0. \tag{A10}$$

With this procedure we can take into account leading order dispersive terms in equations (3) and (4). The full dispersion profile is thus embedded rewriting the linear operator $\tilde{\mathcal{L}}$ as:

$$\tilde{\mathcal{L}}(\omega) = \begin{pmatrix} -\alpha'_1 - i\Delta + i\left(\beta'_{\mathrm{FF}}(\omega) - \beta'_{1,\mathrm{FF}}\omega - \beta'_{0,\mathrm{FF}}\right) \\ -\alpha'_2 - 2i\Delta + i\left(\beta'_{\mathrm{SH}}(\omega) + (\beta'_{1,\mathrm{FF}} - 2\beta'_{1,\mathrm{SH}})\omega - \beta'_{0,\mathrm{SH}}\right) \end{pmatrix}. \tag{A11}$$

A.4 Codes implementation

The numerical implementation of the dynamical models presented in this work, has been fully developed by home-built codes using Julia language [72].